Bulk Scattering Approximations for Collimated Light Transmitted through Paper

by

Tenn Francis Chen

A thesis

presented to the University of Waterloo

in fulfillment of the

thesis requirement for the degree of

Master of Mathematics

in

Computer Science

Waterloo, Ontario, Canada, 2009

I hereby declare that I am the sole author of this thesis. This is a true copy of the thesis, including any required final revisions, as accepted by my examiners.

I understand that my thesis may be made electronically available to the public.

Abstract

Paper is a complex fibrous material whose production involves substantial amounts of natural and industrial resources. To reduce its manufacturing costs, the pulp and paper industry often employs optical technology such as high sensitivity laser sensors used to measure physical parameters like thickness and opacity. More recently, computer simulations of paper optical properties are also being used to accelerate the research cycle required to the development of new types of paper. In these simulations, the bulk scattering of paper is usually approximated by analytical formulas, notably the Henyey-Greenstein function. In this work, we qualitatively investigate the degree of accuracy of such approximations with respect to collimated light. More specifically, an experimental set-up was devised to record the transmission of red and green HeNe lasers through different paper samples. The measured data was compared with data obtained using the Henyey-Greenstein function and data obtained using an alternative exponentiated cosine function. The comparisons are used to qualitatively assess the degree of accuracy of the bulk scattering approximations provided by both functions. This work closes with a discussion on the practical implications of our findings for the modeling of paper optical properties.

Acknowledgments

I would like to give thanks to God for everything, past, present and future. My His will be done on earth, as it is done in heaven.

Next, I would like to thank my advisor, Dr. Gladimir Baranoski. Without his patience and persistence, I would never arrive at where I am today. His academic integrity and unwavering standards make him a great supervisor, while his insightful wisdom and polite mannerisms make him a great friend.

I am very grateful to Dr. K. Frank Lin who provided technical expertise and assistance, without which, this research would not have been possible. I would also like to thank my colleague, Lesley Northam, for providing additional paper samples to broaden the scope of the results in this work.

I would also like to thank the members of my reading committee, Dr. Jeff Orchard and Dr. Paulo Alencar, for they have provided very helpful and valuable insights and suggestions.

Last but not least, my parents, whose love and discipline over the years always keeps me on the right path.

Contents

List of Figures

List of Tables

List of Symbols

Γ	phase function	4
θ	polar angle	4
ϕ	azimuthal angle	4
Γ_{HG}	Henyey-Greenstein phase function	5
g	asymmetry factor in Henyey-Greenstein function	5
Γ_{EC}	exponentiated cosine phase function	5
n	directional exponent in exponentiated cosine function	5
ξ	uniformly distributed random variable in [0, 1)	5
ϕ'	a specific azimuthal angle	7
P	cumulative density function	7
θ'	a specific polar angle	7
$\xi_\circ$	general random variable	7
$\Re$	range of $\xi_\circ$	7
$\Re'$	subregion of $\Re$	7
P_{HG}	cumulative density function for Henyey-Greenstein function	7
P_{EC}	cumulative density function for exponentiated cosine function	8
ξ_i	i^{th} uniformly distributed random variable in [0, 1)	8
Γ'_{HG}	superposition of two different Henyey-Greenstein warping functions	20
$\Gamma_{HG,i}$	i^{th} Henyey-Greenstein warping function	20
u	weight factor in the interval (0, 1) used for Γ'_{HG}	20

Chapter 1

Introduction

In the field of grading paper, many appearance-related attributes are evaluated using optical techniques. Properties like brightness and opacity can be determined through the measurement of light reflection and transmission responses of material samples [13]. Additionally, structural characteristics like roughness and thickness can be evaluated using optical styli [47] and lasers [42]. Recently, computer simulations are also being used to predict paper appearance attributes before manufacturing to mitigate production costs. For example, the effect of dyes and pigments on colour and brightness can be predicted before physical samples are produced.

It is important to note that different approaches can be used to simulate paper optical properties, and no single approach is superior in all cases. While stochastic approaches (*e.g.*, Monte Carlo based models [26, 12]) are known for their flexibility, deterministic approaches (*e.g.*, Kubelka-Munk and discrete ordinate based models [23]) usually require less computational time. Both approaches, however, employ functions to describe the bulk scattering of material samples.

In practice, the choice of a function to describe the bulk scattering of a given material is associated with data constraints. For example, after Bruls and van der Leun [11] suggested that their measurements of the scattering profile of skin tissues could be approximated by

curves obtained using the Henyey-Greenstein (henceforth referred to as HG) function [31], it started to be employed in studies involving light transport in tissues for which measured scattering data is scarce, either by plugging it into the radiative transfer equation [36], or using it to derive warping[1] functions within Monte Carlo modeling frameworks [50].

One technique often employed in Monte Carlo integration is importance sampling [28]. If the integrand is a product of two functions and one of them is known, this function, called importance function or probability density function (PDF), can be used to guide the sampling strategy. In Monte Carlo simulations involving ray optics techniques, the direction of a light ray interacting with a material's internal structures is given by warping functions derived from the integration of the PDF. In short, these functions provide the scattering angles of the propagated ray.

Clearly the selection of an inappropriate PDF to approximate the scattering profile of a material may introduce error in the modeling of its appearance attributes. For example, the HG function is neither based on the mechanistic theory of scattering [36], nor was it originally proposed to represent the bulk scattering of multilayered materials [31]. Furthermore, as stated by Jacques *et al.* [36], "the use of the HG function to specify radiant intensity for thicker samples is only descriptive, and should be distinguished from the customary use of the HG function to describe single particle phase function". Despite these issues, due to its convenient mathematical tractability, it is often employed to approximate the bulk scattering of complex media, including stochastic (*e.g.*, using it as PDF in a Monte Carlo integration [12]) and deterministic (*e.g.*, expanding it using a Legendre polynomial technique in a discrete ordinate formulation [23]) frameworks used to model paper optics properties. As stated by Neuman [46], there is a need for more experimental data that can allow the selection of functions that adequately described the light scattering in paper.

In this work, the accuracy of HG based approximations is investigated. More specifically, data generated using HG based warping functions (HGWF) are compared with

[1]In the context of this investigation, the term "warping" refers to the transformation of uniform to non-uniform distribution of sample rays (directions).

scattering data measured for four different paper samples illuminated by collimated light[2] sources (represented by two different HeNe lasers[3]), as well as data computed using a warping function derived from an exponentiated cosine function (henceforth referred to as ECWF and EC respectively). To the best of our knowledge, none of the current modeling frameworks aimed at paper optical properties employs this function. It is worth mentioning that the main results of this investigation are also available in an open access journal publication [15].

The remainder of this thesis is organized as follows. The next chapter presents the mathematical background of the functions used in this research, and it is followed by a chapter reviewing work related to these functions. Structural characteristics and physical properties affecting the appearance attributes of paper are outlined in Chapter 3. Methods for collecting the physical and simulated data are described in Chapter 5. The closest approximations between the physical and simulated data sets are presented and qualitatively compared in Chapter 6. Finally, in the last chapter, the main conclusions derived from this investigation are summarized and directions for future research are outlined.

[2]Collimated light sources are those that generate light beams in which rays are all nearly parallel [32].

[3]A laser is a device that utilizes the natural oscillations of atoms for amplifying or generating highly monochromatic and coherent, visible radiation [1, 32].

Chapter 2

Mathematical Background

This chapter presents the mathematical background behind the functions used in this investigation. The concept of phase function will first be introduced, followed by a presentation of the specific functions of interest. The corresponding warping functions' derivation and purpose will then be outlined.

2.1 Phase Functions

When a light encounters an optical interface, it is scattered and the direction of its optical path is modified. A phase function, $\Gamma(\theta, \phi)$, can be used to quantify the amount of light that will be scattered in a certain direction at a polar angle $\theta \in (0, \pi)$ and an azimuthal angle $\phi \in (0, 2\pi)$. We will use $\theta = 0$ to denote the original direction of the light before scattering. In this case, the phase function is used to describe the behavior of a single scattering event.

However, phase functions have been used extensively to describe multiple or bulk scattering as well. In this context, phase functions are used as PDFs to describe the behavior of light after interactions at multiple optical interfaces [11, 22, 29]. Thus, given a phase function, the integral over all directions must be equal to the unity.

We bring two items to attention. First, the term "phase function" is somewhat mislead-

ing, since it does not have any connection to the phase of the electromagnetic wave (light). Instead, it has its origins in astronomy, more specifically in the study of lunar phases [35]. Second, the phase functions discussed in this investigation are usually used while assuming azimuthal symmetry, *i.e.*, scattering is uniform in the azimuthal direction [12, 50, 22]. Thus, for the remainder of this thesis, we will omit the azimuthal component of the phase function and write $\Gamma(\theta)$ to mean $\Gamma(\theta, \phi)$.

The HG phase function can be written as [31]

$$\Gamma_{HG}(\theta) = \frac{1}{4\pi} \frac{1 - g^2}{(1 + g^2 - 2g \cdot \cos\theta)^{3/2}}, \tag{2.1}$$

where g is the asymmetry factor ranging from -1 to 1. For negative values of g, the function simulates back scattering; 0, symmetric scattering; and positive, forward scattering.

The EC phase function is defined as [7]

$$\Gamma_{EC}(\theta) = \frac{n + 1}{2\pi} \cos^n \theta, \tag{2.2}$$

where n is the directional (specular) exponent. We note that the EC function was originally designed to describe light propagation in the forward direction, and was defined only in the domains $0 \leq \theta \leq \frac{\pi}{2}$ and $n \in (0, \infty)$. We will follow the same convention in this thesis. Like g, a greater n would represent greater forward scattering. The effect of these parameters are shown in Figures 2.1 and 2.2.

2.2 Warping Functions

At each bulk scattering event in a Monte Carlo simulation, a direction needs to be randomly selected in accordance with the probability density functions. This can be done by choosing a uniformly distributed random variable $\xi \in [0, 1)$, and then *warping* it to conform with a phase function's distribution.

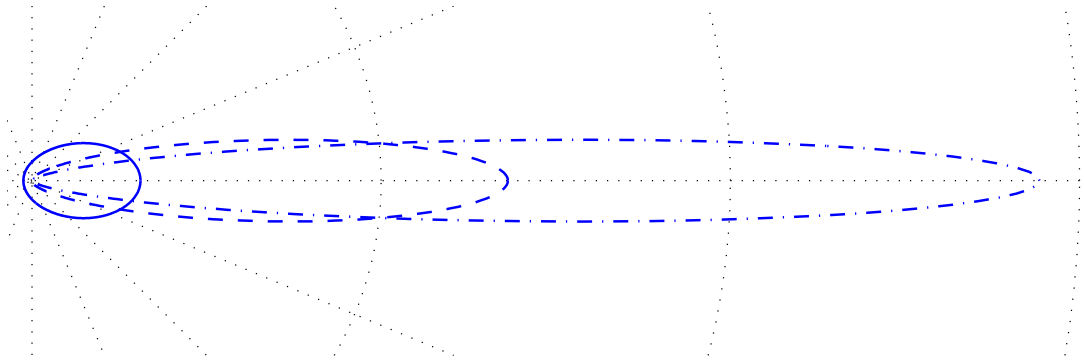

Figure 2.1: Probabilities densities given by the Henyey-Greenstein phase function parameterized by different values of g. The values of g from least to most forward scattering are 0.4 (solid line), 0.8 (dashed line) and 0.9 (dot-dashed line).

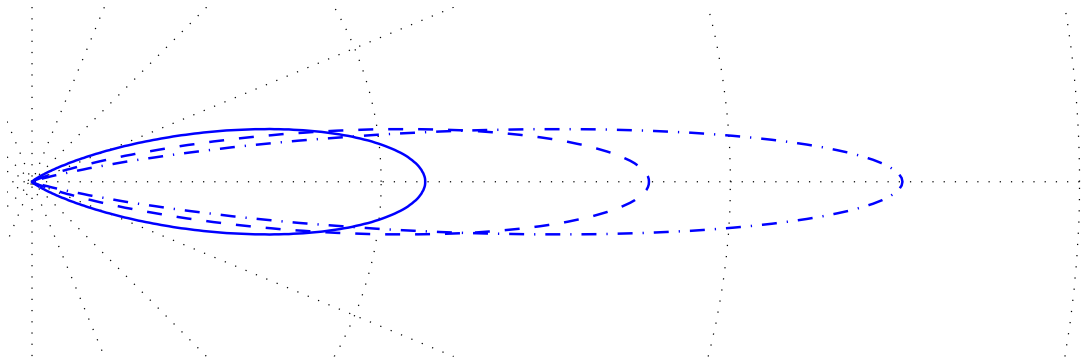

Figure 2.2: Probabilities densities given by the exponentiated cosine phase function parameterized by different values of n. The values of n from least to most forward scattering are 20 (solid line), 50 (dashed line) and 100 (dot-dashed line).

We first consider the simpler case of the azimuthal symmetry assumption. In this case, the probability density function is a uniform distribution. Then, a specific random azimuthal angle can be generated by

$$\phi' = 2\pi\xi. \tag{2.3}$$

Equation 2.3 is an example of a warping function.

For the polar angles, the warping functions are not as intuitive. We derive them by first stating their cumulative density function $P(\theta < \theta')$ as an integral of the PDF.

Given a random variable $\xi_\circ$ defined over some region $\Re$, then the probability that $\xi_\circ$ will take on a value in subregion $\Re' \subset \Re$ is given by [7]

$$P(\xi_\circ \in \Re') = \int_{\xi_\circ \in \Re'} \Gamma(\xi_\circ) d\zeta(\xi_\circ).$$

In computer graphics, $\Re$ is typically an area ($d\zeta = dx\ dy$) or, as in our case, a set of directions ($d\zeta = \sin\theta\ d\theta\ d\phi$) [7].

Then, the warping function for the HG function can then be derived [6] by first stating the probability of generating an angle smaller than some specific angle θ' [7]:

$$\begin{aligned} P_{HG}(\theta < \theta') &= \int_0^{2\pi} \int_0^{\theta'} \Gamma_{HG}(\theta)\ \sin\theta\ d\theta\ d\phi \\ &= \int_0^{2\pi} \int_0^{\theta'} \frac{1}{4\pi} \frac{1-g^2}{(1+g^2-2g\cdot\cos\theta)^{3/2}} \sin\theta\ d\theta\ d\phi. \end{aligned}$$

Evaluating the above results in

$$P_{HG}(\theta < \theta') = \frac{1-g^2}{2g}\left(\frac{1}{1-g} - \frac{1}{\sqrt{1+g^2-2g\ \cos\theta'}}\right).$$

We equate $P_{HG}(\theta < \theta')$ to a uniformly random variable ξ and solve for θ' resulting in

$$\theta' = \arccos\left(\frac{1}{2g}\left(1 + g^2 - \left(\frac{1 - g^2}{1 + g - 2g\xi}\right)^2\right)\right), \tag{2.4}$$

which effectively corresponds to the warping function for HG with respect to the polar angle.

Similar steps can be taken for EC to derive its corresponding warping function [7]. Again, we start with the probability, in terms of an integral, which is given by

$$\begin{aligned} P_{EC}(\theta < \theta') &= \int_0^{2\pi} \int_0^{\theta'} \Gamma_{EC}(\theta)\ \sin\theta\ d\theta\ d\phi \\ &= \int_0^{2\pi} \int_0^{\theta'} \frac{n+1}{2\pi} \cos^n\theta\ \sin\theta\ d\theta\ d\phi. \end{aligned}$$

Then, evaluating the integral yields

$$P_{EC}(\theta < \theta') = -\cos^{n+1}(\theta') + 1.$$

We again set this equal to a uniformly random variable ξ and solve for θ' resulting in

$$\theta' = \arccos\left((1 - \xi)^{\frac{1}{n+1}}\right), \tag{2.5}$$

which effectively corresponds to the warping for EC with respect to the polar angle.

Now, these warping functions can be used to generate a set of directions that follow the distributions given by the HG or EC functions. For each random direction, we generate two uniformly random numbers in [0, 1) and then substitute them into the desired warping functions. For example, to generate a ray according to the HG function, we generate uniformly distributed random variables ξ_1, $\xi_2 \in [0, 1)$ and obtain the azimuthal angle from Equation 2.3 using ξ_1 and a polar angle from Equation 2.4 using ξ_2.

Chapter 3

Paper Structural Characteristics and Physical Properties

This chapter briefly outlines the main structural characteristics and physical properties of paper that affect its appearance attributes. An emphasis is given on characteristics and properties directly related to the spatial distribution (scattering) of light, which determine, among other attributes, the degree of translucency[1] of paper samples (Figure 3.1).

3.1 Fibers

Paper is primarily composed of cellulose fibers [18]. Cellulose is a chemical compound which exists in varying degrees of purity in various plants [14]. Paper makers need to purify cellulose since too much impurity would compromise the quality of the pulp. Alpha cellulose can be considered the "pure" cellulose component. It is not a substance, but rather, a portion of cellulose empirically determined through chemical analysis. Beta and gamma cellulose are determined in a similar way, but are considered to be less pure.

[1] Almost all commercial papers are translucent. Translucency is the property of a specimen by which it transmits light diffusely without permitting a clear view of objects beyond the specimen and not in contact with it [21].

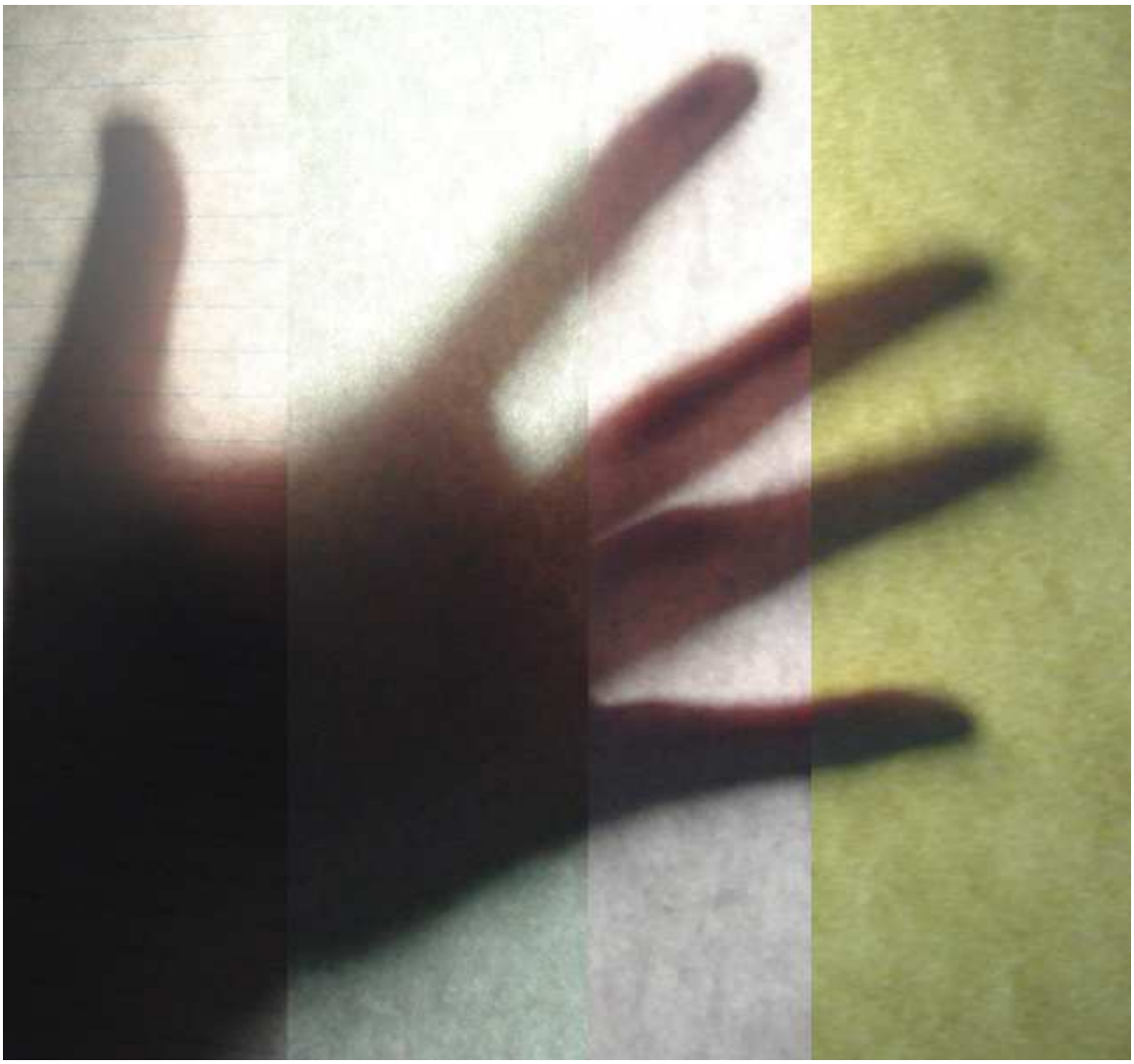

Figure 3.1: Photographic composition illustrating the translucency of different types of paper.

3.1.1 Flocculation

Flocculation is defined as a process where some substance or material forms clumps. In paper, this can be seen as a non-uniform distribution of the fibers' centers. To the naked eye, this would affect the uniformity of the paper. Figure 3.2 contains a sketch that demonstrates this phenomenon. Figure 3.3 is a microscope image showing flocculated fibers within a sheet of lens paper. In general, papermakers strive to limit flocculation to produce uniform looking papers [17].

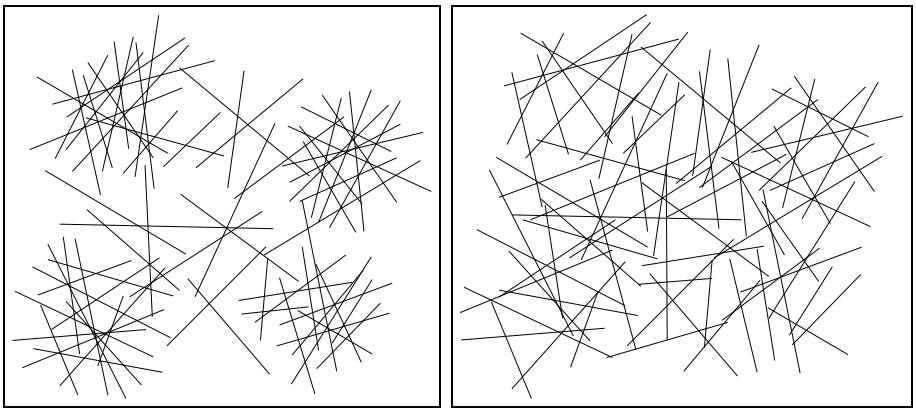

Figure 3.2: Flocculation: Flocculated straight lines (left). Unflocculated straight lines (right).

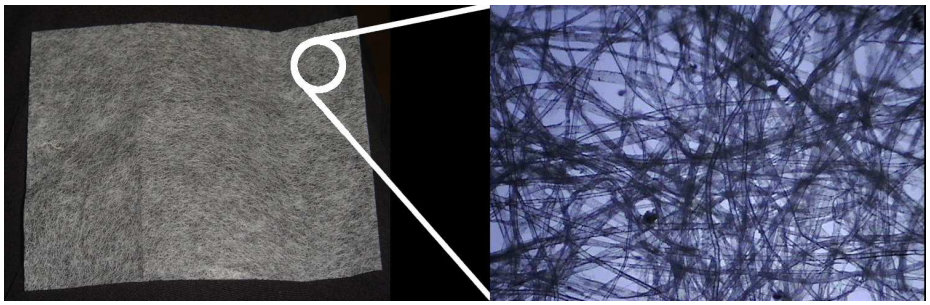

Figure 3.3: A microscope image showing fibers from a sheet of lens paper. We can see fiber flocculation as dark concentration of fibers near the left and upper-center portions of the image.

3.1.2 Orientation

While flocculation addresses the position of the fibers, orientation address the rotation of the fibers. Note that it is usually easier to tear along long rather than short direction in a sheet of paper. One would then suspect the fibers being aligned along the length of the page [18]. This suspicion can be confirmed by the typical distribution of the orientation of the fibers [17]. Figure 3.4 is a plot of the fiber orientation distribution of a typical sheet of paper, while Figure 3.5 contrasts two extreme cases of orientation. This difference in orientation may also affect the anisotropy[2] of the optical properties of paper [25].

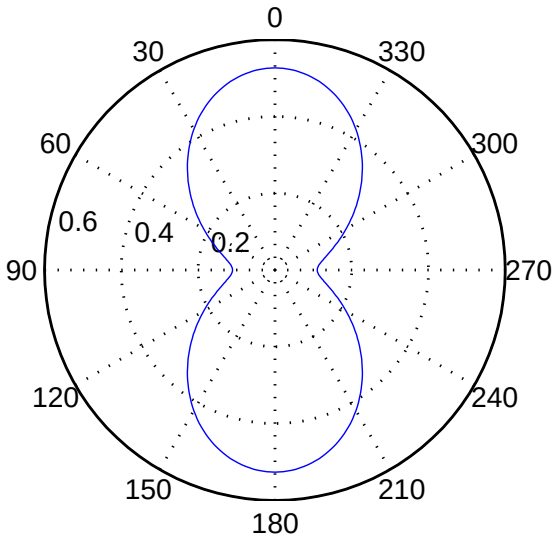

Figure 3.4: A polar plot of the probability distribution of fiber orientation given by $p(\theta) = \frac{1}{\pi} + 0.208\ \cos(2\theta)$ with 0° degrees being the machine direction (Machine direction is the direction of how the fibers are fed into the rollers during paper manufacturing [13]). Redrawn from [17].

[2]Anisotropy in this (external) context is defined as follows. When illumination and viewing directions are kept constant, and the material is rotated about its normal, if the intensity of light observed by the viewer varies, then the material is considered to be anisotropic. Otherwise, the material is considered to be isotropic [7].

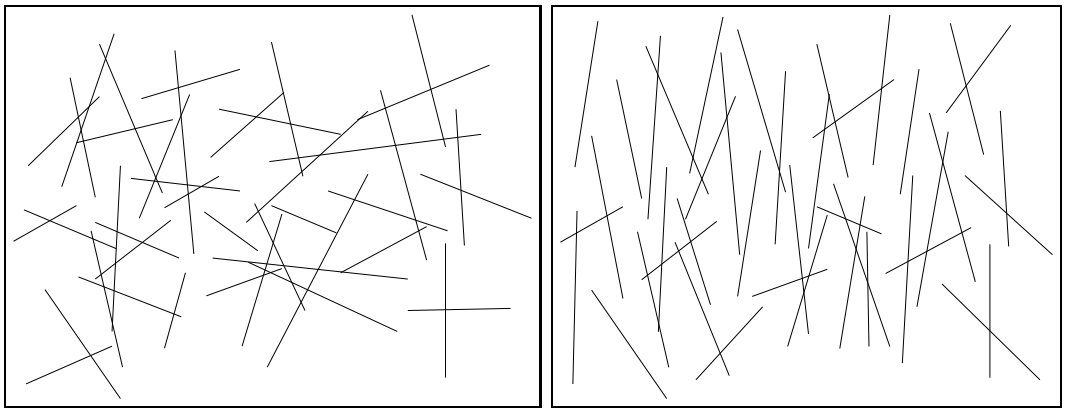

Figure 3.5: Fiber Orientation: Uniformly oriented straight lines (left). Non-uniformly oriented straight lines (right).

3.2 Solid Fraction

Solid fraction is the percent of the paper's volume that is occupied by the solid composition of the paper [2]. This value is not easy to measure, and may require chemical analysis or gas expansion methods to obtain [2].

When all other factors are constant, it is qualitatively difficult to predict whether a paper should be more or less transparent due to differences in solid fraction. When a paper has a very low solid fraction, its properties would be similar to air, and be relatively transparent. Thus, as the paper is compressed more, becoming more dense, the paper would become less transparent. However, after a certain point, the compression would result in more optical contact between the fibers, decreasing the amount of light scattering interfaces. At the extreme theoretical case of maximum compression, the paper would become a pure block of cellulose, containing minimal optical interfaces. Since cellulose itself is relative transparent, this compressed paper would also have very low opacity[3] [13]. Figure 3.6 presents data that illustrates this fact by relating physical measurements of contrast ratio[4] as a function of solid fraction.

[3]Opacity is defined as the reciprocal of the amount of light transmission [13]. A perfectly opaque paper would be impervious to all visible light.

[4]Contrast ratio is a way to measure opacity, defined as the ratio between the reflectance when backed by a black surface over the reflectance when backed by a white surface [13].

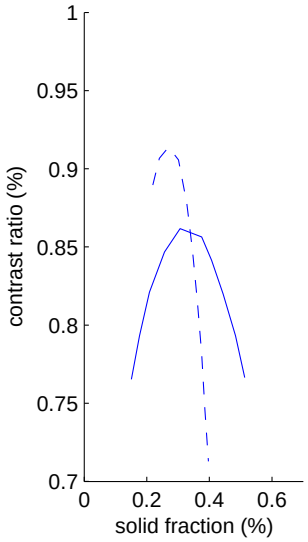

Figure 3.6: A plot of the effect of solid fraction on contrast ratio for paper basis weight 45 pounds (solid line) and 20 pounds (dashed line). See Section 3.3 for definition of basis weight. Redrawn from [20].

3.3 Basis Weight

Basis weight is arguably the most important property of paper from a commercial standpoint. Most paper is sold based on this property [13]. Technically, it is the measure of the paper's mass per area. Density is also defined for paper but basis weight is usually used since the usable area of paper is more important than the actual volume of the paper. In the paper industry, basis weight is measured as the weight of a ream at the paper's basic sheet size, where a ream is 480 or 500 sheets.

A smaller basis weight would imply less mass per area. Intuitively, this would also infer a decrease in thickness, strength and, most relevant to us, the opacity. However, caution should be exercised when using basis weight for the analysis of optical measurements. For example, an increase in basis weight may be correlated with increase in solid fraction, which can increase or decrease opacity (see section 3.2).

3.4 Dyes, Pigments and Optical Whiteners

Although not a property of the paper itself, dyes, pigments and optical whiteners are frequently used to alter the appearance attributes of paper, especially those related to color.

Cellulose fiber in its raw form is slightly yellow white but people prefer slightly blue white. Therefore, the purpose of many artificial colours is to increase the blue reflectance of the paper. Dyes and pigments accomplish this task, but they technically decrease overall whiteness by absorbing the light of non-blue wavelengths [13]. This effect can be reduced or eliminated by including submicron-sized particles like titanium oxide whose refractive index greatly differs from that of the surrounding medium. The presence of these particles will increase overall diffuse light reflection [16, 24]. Even if the reflectance is reduced, the slightly more uniform spectral reflectance would appear whiter to the human visual system [30].

Dyes and pigments also have an effect on the opacity of paper. Dyes will increase opacity by absorbing light. Pigments can increase opacity by absorbing and increasing scattering. However, some pigments can also decrease opacity if they fill the paper and decrease air-fiber interfaces by increasing pigment-fiber interfaces. This is due to the refractive index of pigments being closer to that of the fibers, and so the pigment-fiber interfaces will decrease overall light scattering.

Optical whiteners, also known as florescent dyes, optical bleaches or whiteners, are different from dyes in that they can actually brighten the paper and not just appear to whiten paper [13, 30]. They accomplish this task by absorbing light from the invisible ultraviolet end of the spectrum, and reemitting it as visible blue light. However, these dyes fade fast, and rarely keep paper looking new for long. Also, whiteners depend on ultraviolet light, so paper may not look as white when indoors, or look blue or purple under sunlight.

The modification of reflectance discussed in this section by normal and florescent dyes is illustrated in Figure 3.7.

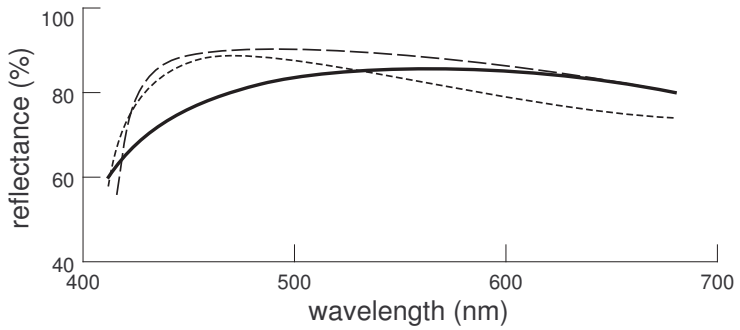

Figure 3.7: A sketch plot of the reflectance of hypothetical fibers (solid line) and how it might be modified by normal (dotted line) and florescent (dashed line) dyes. Based on graph provided in [13].

Chapter 4

Related Work

This chapter will concisely review various applications of the HG and EC functions in related fields and works addressing to the shortcomings of such applications.

4.1 Henyey-Greenstein Function

The HG function was first presented in 1941 by Henyey and Greenstein in the astrophysical literature [31]. It was employed to approximate Mie scattering[1] in the study of diffuse radiation in galaxies [6]. It has no physical basis, and was introduced to fit scattering data of stellar radiation. However, it has since been widely used in many different fields that require light scattering approximations due to its mathematical tractability.

4.1.1 Biomedical Optics

One field that has seen extensive use of the HG function is biomedical optics. Bruls and van der Leun [11] introduced it to this field by performing goniometric measurements of the outermost layers of human skin, specifically the stratum corneum and epidermis, and then suggesting the use of the HG function to approximate the scattering profile of skin

[1]Mie scattering occurs when the size of the participating medium compared to the wavelength of light is on the same magnitude [8]. In this situation, traditional ray optics techniques cannot be applied.

tissues. Following in his footsteps, Jacques *et al.* [36] and Yoon *et al.* [60] applied the same function to approximate the scattering profile of the skin dermis and human aorta, respectively. These investigations were conducted with specific medical applications in mind and used a red HeNe laser at 633 nm. Prahl *et al.* [50, 51] was motivated by these works and incorporated the HG function to a Monte Carlo-based algorithm to study light transport in tissue during laser irradiation.

Bruls and van der Leun's original measurements were examined by van Gemert *et al.* [58], and it was concluded that the HG function provided a good description for the investigated tissue samples. Since then, it is generally assumed that the HG function could be used to approximate the scattering profile of organic tissues. For example, its use in tissue optics for analytical and Monte Carlo models of light propagation simulations are widespread in this field [56].

4.1.2 Computer Graphics

The computer graphics community is also interested in light interaction with organic tissues. For example, to create more realistic virtual actors, a good model for skin is highly desirable. Hanrahan and Krueger [29] and Stam [54] both used the HG function as a component in their light scattering models to address this challenge.

Although Stam's model was specifically directed at rendering skin, Hanrahan and Krueger's model was presented as a general subsurface scattering model employing a Monte Carlo light transport algorithm (previously presented in the biomedical literature by Prahl *et al.* [49, 50]) that could also model other organic materials such as plant leaves. In their model, materials are modeled as layers, and scattering events occur at random positions within a layer. The directional changes of light occurring at these scattering events are simulated by the HG function.

In his model [54], Stam represents light interaction with skin as multiple scattering events within a layer bounded by two rough surfaces. The skin tissue itself is modeled

as a uniform material. The HG function was then applied to a discrete-ordinate radiance transfer equation describing this geometry to infer the appearance of skin.

However, the use of the HG function was not limited to organic materials. Stam noted that the aim of his model is to simulate the appearance of natural materials including snow, sand and paint. Dorsey *et al.* [19] also used the function to render weathered stone, and Jensen *et al.* [38] employed the use of the HG function to render various materials, including wet and dry paper. Jensen *et al.* [37] also applied it to visualize clouds in night scenes. In these models, the function is used to simulate multiple subsurface scattering within the medium.

4.1.3 Paper Optics

Within the optics community, with a more quantitative and predictive mindset, Carlsson *et al.* [12] used the function to simulate light scattering within paper using a Monte Carlo simulation. They first shined lasers of different wavelengths through papers of various basis weight[2] and measured the time difference between laser emission and detection. This time delay was used to determine the optical pathlenght of the transmitted light due to scattering. A model was then constructed where paper was assumed to be layers of cellulose in air. Light scattering was assumed to occur only at the cellulose-air interfaces and follow the distribution given by the HG function. Using this assumption, Carlsson *et al.* determined the best asymmetry factors that yielded the closest approximations to the experimental data, and inferred the mean scattering angles occurring in the paper simulations.

Edström's discrete ordinate modeling package, DORT2002 [22], was specifically designed for predictive simulations of paper for use in the paper industry. It also uses the HG function. The model's geometry is similar to that used by Carlsson: plane parallel material layers. However, instead of using a Monte Carlo approach to the simulations,

[2]See Section 3.3 for definition of basis weight.

Edström uses discrete ordinate methods to approximate solutions to the radiative transfer equation. Users of the model can define distinct layers characterized by thickness, scattering and absorption coefficients, and a function to describe the scattering. Although the user can define different functions, the HG function is presented as the default.

4.1.4 Applicability

We first note that the HG function cannot be used to describe simultaneous forward and backward scattering which are typical in many cases of Mie scattering [4]. However, many researchers have accommodated for this by proposing variations based on the superposition of two HG phase functions, given by

$$\Gamma'_{HG} = u\Gamma_{HG,1} + (1-u)\Gamma_{HG,2},$$

where $\Gamma_{HG,1}$ and $\Gamma_{HG,2}$ are both HG functions defined by Equation 2.1 but parameterized by different asymmetry factors, and u is a weight factor from the interval (0, 1). Examples of researchers that have employed this strategy include Irvin [34], Kattawar [39], Uesugi *et al.* [57] and Witt [59], and more recently, Dorsey *et al.* [19] and Jensen *et al.* [38]. Other similar ideas include the use of other functions in the superposition, such as replacing one of the HG functions with the isotropic[3] function [36].

However, despite its flexibility and adoption in numerous applications, the correctness of the HG functions is still a topic of interest among researchers from various fields, including biomedical optics [5, 45], remote sensing [44] and computer graphics [6]. Within biomedical optics, the generalized use of the HG function has not been broadly examined since the study by van Gemert *et al.* [58], despite the growing uncertainty about its accuracy. A specific example of a shortcoming is the function underestimates the amount of scattering of mammalian cell suspensions under certain conditions [45].

[3]Isotropy in this (internal) context indicates that light is distributed symmetrically in all directions within the medium [7].

Additionally, a common issue with many of the models presented above is the use of the asymmetry factor. The HG function is an empirical function characterized by this single parameter which bears no physical relation to the material being simulated. For example, in the rendering of dry paper by Jensen *et al.* [38], they used the superposition of the HG functions and with the asymmetry factors 0.05 and -0.05, and a weight factor 0.2. It was not clear how these parameters are connected to the actual paper being rendered, namely, the only property described being thickness equal to 0.8 mm. A similar issue exist in his rendering of the wet paper as there were no clear mapping between water saturation and the corresponding parameter values.

Results by Carlsson *et al.* [12] also show no clear relationship between the simulation and physical properties. Although values of g were obtained that could explain the optical path length of the transmitted lasers, no mathematical relation was proposed with the actual lasers' wavelengths and the papers' basis weight.

As briefly described above, the HG function was initially used in optics just as a function to fit multiple scattering data measured at specific wavelengths. Since then, it has been adapted to various fields with questionable applicability. At the core of these issues is the fact that the HG function has no direct connection with the underlying physical phenomena being studied, which may negatively affect the predictability of any simulation that employs it.

4.2 Exponentiated Cosine Function

The function we present as an alternative to the HG function is the EC function. This function was first introduced in a reflectance model in the computer graphics community by Phong in 1975 to quantify the specular component [48]. Since then, it has been applied to numerous different fields as well. For example, Brakke *et al.* [10] noted the scattering profile of plant leaves approaches that given by the exponentiated cosine function.

This observation has triggered the incorporation of this function into predictive models of light interaction with organic [3] and inorganic [40] materials. This function has also been used to render diffuse light transmission through translucent materials such as paper lampshades [52].

The EC function is similar to the HG function in sharing many of the same advantages and disadvantages. They are both straightforward to implement and apply in different models with the function behaviour dictated by one parameter. Furthermore, the original formulation of the EC function is not suitable for physically-based rendering applications since it did not account for the conservation of energy [7]. It was later constrained by Immel *et al.* [33] and Lewis [43] to become physically plausible. A constrained version of this function (Equation 2.2), often used by stochastic models of light interaction with matter (*e.g.*, [7, 40]) to derive the corresponding warping functions, is also used in this investigation (Equations 2.3 and 2.5).

Chapter 5

Experimental Materials and Methods

This chapter presents the materials and methods used to collect the physical and simulated data used in this work. The physical design of the physical experiment will be presented first, followed by the explanations of the strategies used in the simulations.

5.1 Physical Measurement Set-Up

The set-up used in this investigation was selected because of its low cost/effectiveness ratio. It allows us to obtain reliable data to be used in the qualitative comparisons presented in this work. It is also relatively simple to assemble, which facilitates the reproducibility of the results. In fact, similar set-ups based on the use of a CCD camera and lasers have been chosen in other studies tackling related optical questions. For example, Oksman [47] used a CCD camera to capture images of paper to determine reflectance under different pressures. Carlsson [12] used a CCD device to determine the time delay of the laser transmission at different wavelengths and infer the spectral reflection and transmission of different paper samples. Béland and Bennet [9] used a CCD camera in conjunction with scatterometry techniques to assess the effect of microroughness on glossy papers. The reader interested in more complex set-ups used to obtain highly accurate scattering measurements is referred to a comprehensive book on this topic [55].

The raw measurement data were collected as images of laser transmitted through pieces of different paper samples. For each type of paper, multiple images were obtained, each from a different random position from the paper sample. These photos were all taken in a dark room to eliminate contributions introduced by unwanted light sources. The lasers employed in this investigation were a red 1.07 mW low-power HeNe laser at 633 nm and a green 0.5 mW low-power HeNe laser at 543 nm. To prevent saturation in the images, the intensities of the lasers were limited by a neutral density filter placed at the exit window. A Canon PowerShot S5 IS digital camera was then used to capture images of the transmitted light. The settings used when taking the photographs were 2.48 second shutter speed, $f/3.5$ lense aperture and 400 ISO. The camera was also set to apply minimal post-processing in the images so that linear sensor sensitivity is reflect in the collected data. The set-up of the experiment is illustrated in Figure 5.1.

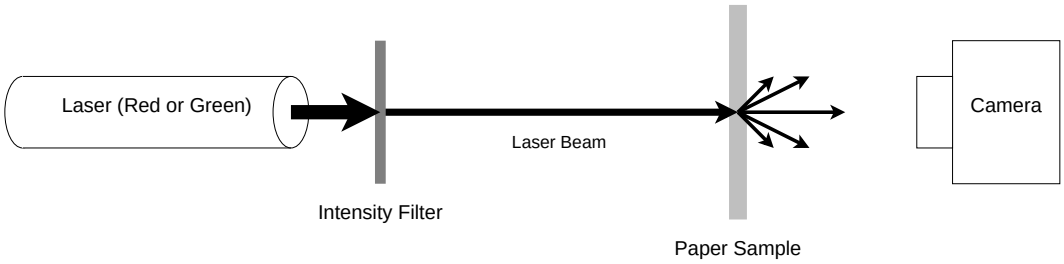

Figure 5.1: Sketch of the physical measurement set-up used to collect the scattering data used in this investigation.

The paper samples used in this investigation were a sheet of lined paper from Hilroy white wide ruled letter pads, a sheet of Staples multiuse 20 lb acid free paper, a sheet of Heinz Jordan Acryloil Series 401 acid free illustrator's paper and a sheet of 140 lb acid free watercolor paper. These paper samples will henceforth be referred to as lined paper, printer paper, sketch paper and water paper respectively. These papers were selected for their differing characteristics with thickness being the most qualitatively apparent. With this characteristic in mind, from the thinnest to thickest, the samples are ordered as follows: lined paper, printer paper, sketch paper and water paper.

Since the primary interest is in the spatial distribution of propagated light, the trans-

mitted laser intensities were radially collected and averaged. The resulting values were then normalized and plotted as a function of the distance (in pixels) from the center of the laser beam. This in effect calibrated the data against the dark frame of the camera, and reduced the effect of any noise that might be present in the images. Figures 5.2 and 5.3 show these plots for the red and green lasers respectively. Due to the finite width of the beam, the central portion of the intensity profile, represented as the partition left of the vertical line in the plots, is characterized by relatively small fluctuations. Hence the focus of this investigation is directed toward the decay in intensity near the edges of the laser beam, marked as the region right of the vertical dashed line, which is associated with the most significant changes in the spatial distribution of propagated light. For each laser, the regions are kept with the same boundaries to ensure a fair comparison within each laser trial. The plots were then normalized to the maximum and minimum value in these regions. We remark that the results obtained using the two different lasers should be analyzed independently of one another since their corresponding physical measurement set-ups may contain minor inconsistencies due to the handling of the different emitters.

5.2 Simulation Approach

Data for each simulation instance was obtained by generating 10^7 rays in conjunction with the corresponding warping functions given in Chapter 2: Equations 2.3 and 2.1 for the HG function and Equations 2.3 and 2.2 for the EC function.

The generated rays were collected using a virtual goniophotometric measurements [41], which are designed to simulate actual devices, known as goniophotometers (see Appendix A), used to measure spatial light distribution. The collection hemisphere was divided into 30 intervals in the azimuthal component and 90 intervals along the polar component. The number of rays, coupled with the strong forward scattering of the simulations, ensured asymptotically convergent readings [41].

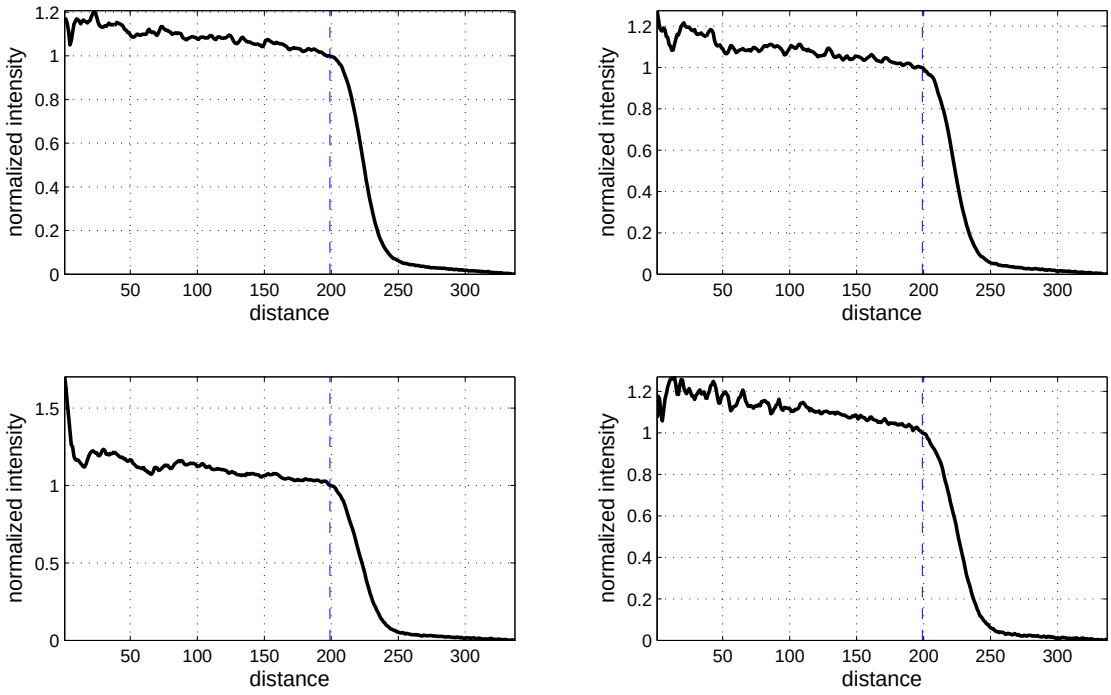

Figure 5.2: Normalized intensity profiles of the paper samples using the red HeNe laser (633 nm). Top left: lined paper. Top right: printer paper. Bottom left: sketch paper. Bottom right: water paper. The dashed lines indicate the beginning of region of interest, and each data set is normalized to the maximum in the region. The distance is given in terms of the number of pixels between the position and the center of the laser beam in the image.

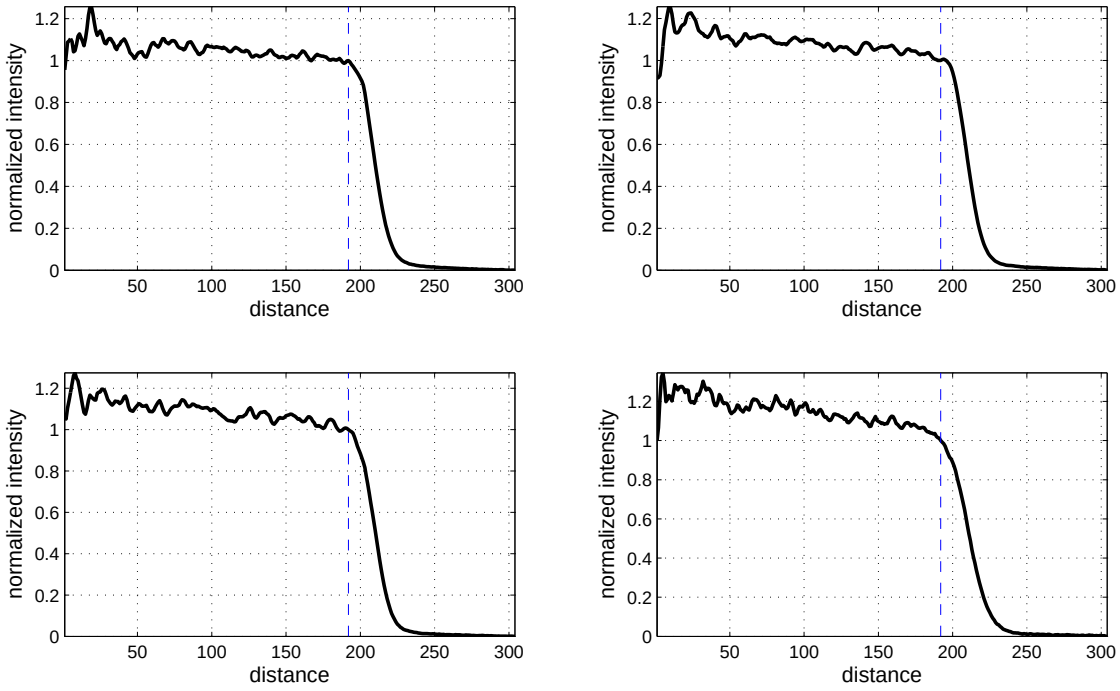

Figure 5.3: Normalized intensity profiles of the paper samples using the green HeNe laser (543 nm). Top left: lined paper. Top right: printer paper. Bottom left: sketch paper. Bottom right: water paper. The dashed lines indicate the beginning of region of interest, and each data set is normalized to the maximum in the region. The distance is given in terms of the number of pixels between the position and the center of the laser beam in the image.

Since azimuthal symmetry was assumed while using the warping functions, the azimuthal intervals were separated evenly. However, it was noted that some subdivision schemes for the polar intervals, such as equal solid angles suggested by Krishnaswamy *et al.* [41], did not provide enough resolution to capture highly directional scattering distributions along the material's normal. Instead, the azimuthal intervals was divided according to a sine distribution. Such a distribution results in more patches near the top of the collector hemisphere, which, in turn, increases the precision of measurements depicting forward scattering profiles such as those investigated in this work. The differences in these two patch distribution schemes are illustrated in Figure 5.4 and the differences in representing the same scattering profiles are shown in Figure 5.5.

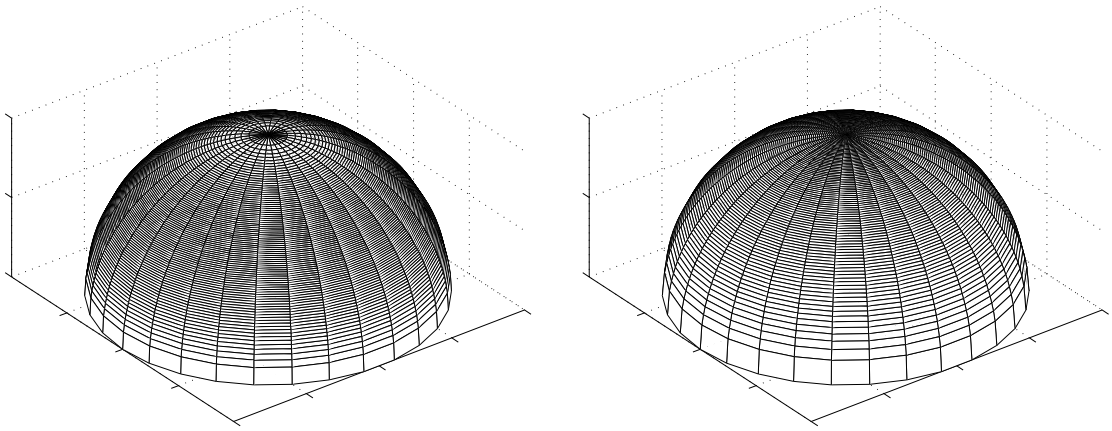

Figure 5.4: Comparison of different hemisphere subdivision schemes for the virtual goniophotometer. Polar intervals divided according to equal solid angles (left) and according to a sine distribution (right). Both of these examples contain 30 azimuthal components and 90 polar components. The most notable difference is near the top of the hemispheres where the subdivisions in the right figure converges to a point.

The simulated data was collected[1] as the intensity as a function of all possible forward scattering directions ($\theta \in [0, \frac{\pi}{2}]$ and $\phi \in [0, 2\pi)$). Like the physical data, the simulated data was then also radially averaged, resulting in the simulated intensities which depend only on the polar angle.

A conversion was required from angle to distance in order to compare against the

[1]The simulated data collected was actually the bidirectional transmittance distribution function (See Appendix B).

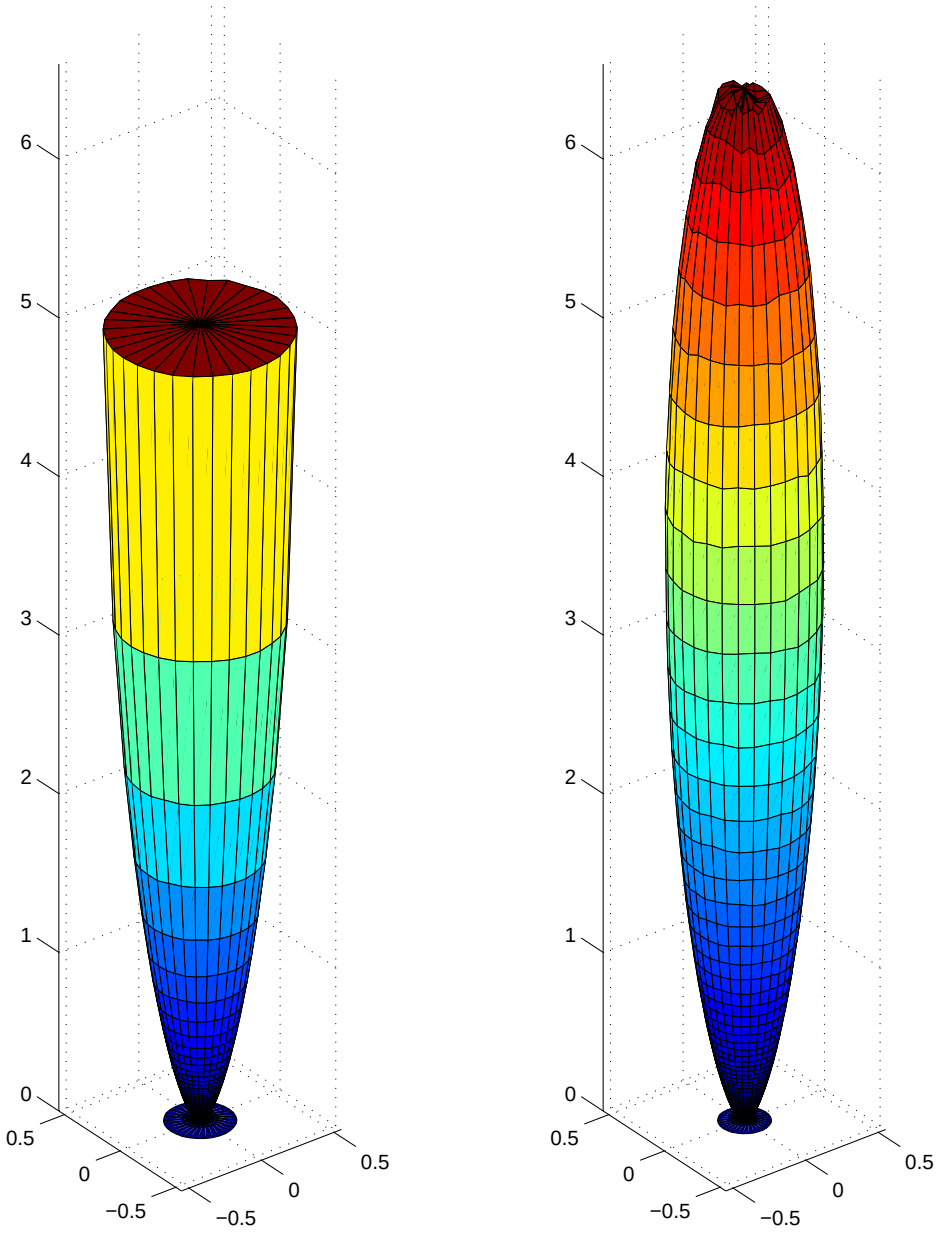

Figure 5.5: Comparison of the same scattering profiles (HG function with $g = 0.85$) collected using different hemisphere subdivision schemes for the virtual goniophotometer. Polar intervals divided according to equal solid angles (left) and according to a sine distribution (right).

measured data, which was collected as intensity as a function of distance. Assuming the raw simulated data is $\rho_\circ$, then the converted data ρ is obtained via the relation

$$\rho(\tan\theta) = \rho_\circ(\theta).$$

However, note that $\tan(\frac{\pi}{2}) = \infty$, and thus, the measured profiles can only be compared against a portion of the simulated profiles. This was accounted for by introducing a horizontal scaling factor to the simulated data in order to ensure the data sets were of the same magnitude, and then truncating the simulated data. This truncated distance is normalized to the unity. The maximum value in the simulated data was normalized to the unity as well.

5.3 Comparison Procedure

The selection of the parameters g and n involved two stages. Initially, a coarse exploration of their space of values is performed to determine the ranges that yield the closer approximations with the data obtained in the physical measurement set-up. The parameter searching process is then refined within these ranges to obtain the best approximation. At the end, the parameter space explored for g was 0.0001 to 0.9999 in refined steps of 0.0001, and the parameter space explored for n was 1 to 500 with refined steps of 1. The best approximation was the one that yielded the smallest root mean square (RMS) error defined as [53]

$$\delta(A, B) = \sqrt{\frac{\sum_{i=1}^{N}(a_i - b_i)^2}{N}}$$

for two data sets A and B where a_i and b_i are the i^{th} value of the A and B respectively, each with N values.

Chapter 6

Results

Figure 6.1 presents the graphs depicting the closest agreements obtained between the measured and simulated data sets for the red laser. Orthogonal plots that further illustrate the differences of these data sets are shown in Figures 6.2 to 6.5. Figures 6.6 to 6.10 present the corresponding results for the green laser. The graphs show that none of the approximations completely agree with their corresponding measured data, with the larger deviations occurring in the region near the inflexion point of these curves. In general, the HGWF does not conform to the relatively sharp bend at the normalized distance between 0.2 and 0.5. This is seen as an overall brighter image and more diffuse dot in the orthogonal plots. However, the ECWF falls off too quickly, for normalized distance greater than 0.4, although this differs on a much smaller scale.

Comparing the results provided by the two warping functions, one can verify the EC data sets present the closer qualitative and quantitative agreement with the actual sets. The later observation is confirmed by the RMS errors presented in Tables 6.1 and 6.2.

Also note that the parameters resulting in the best matches do not correlate with the thickness of the paper samples. As the paper samples become thicker, the absolute intensity of the measured data decreases, and the parameters would be expected to decrease as well. However, neither g nor n decreases monotonically across the measurements for the same

laser.

It is worth mentioning that the ECWF is approximately 40% more expensive than the HGWF. This figure is based on the elapsed CPU time required for their computation on the SGI Onyx 3200 used in our investigation.

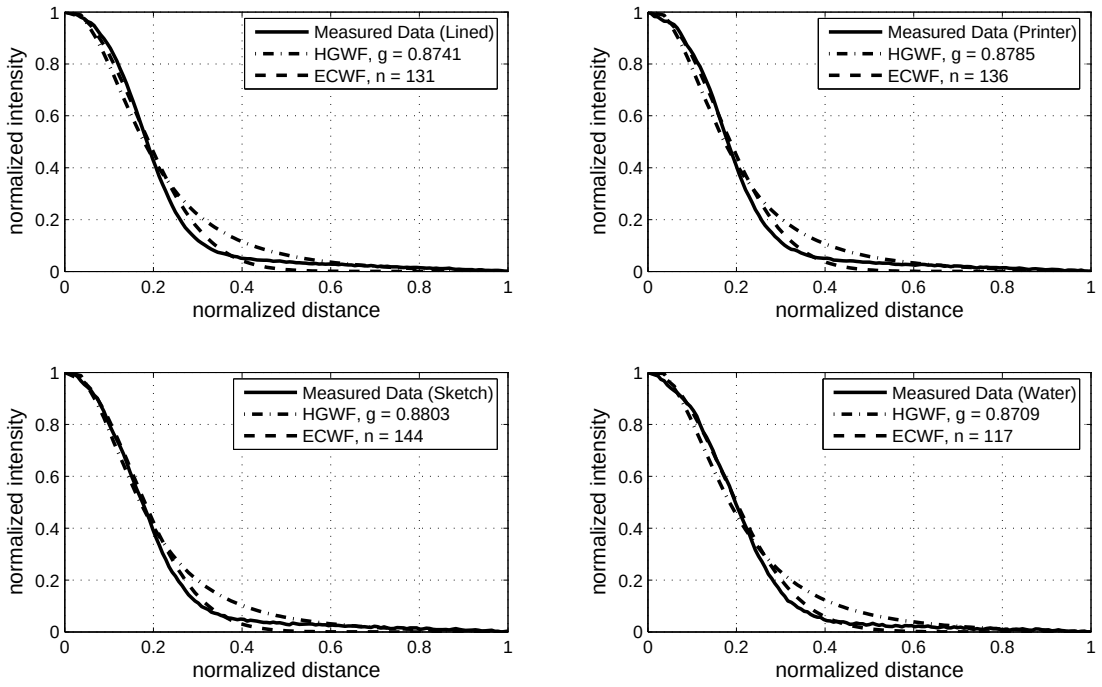

Figure 6.1: Comparison of measured data using the red laser (633 nm) and simulated scattering profiles obtained using the HGWF and ECWF that yield the closest agreements. Top left: lined paper. Top right: printer paper. Bottom left: sketch paper. Bottom right: water paper.

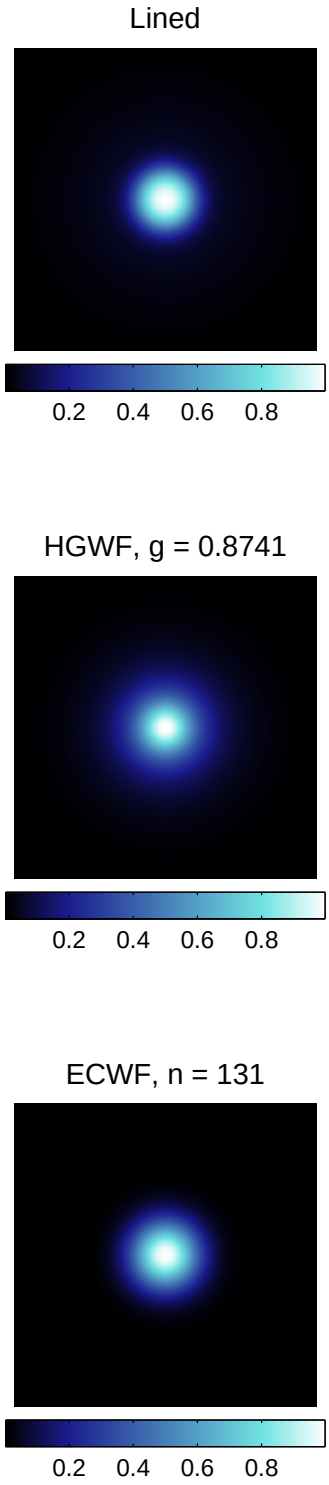

Figure 6.2: Orthogonal projections of scattering profiles, from Figure 6.1, corresponding to data obtained from lined paper using the red laser (633 nm) and its closest agreements using the HGWF and ECWF.

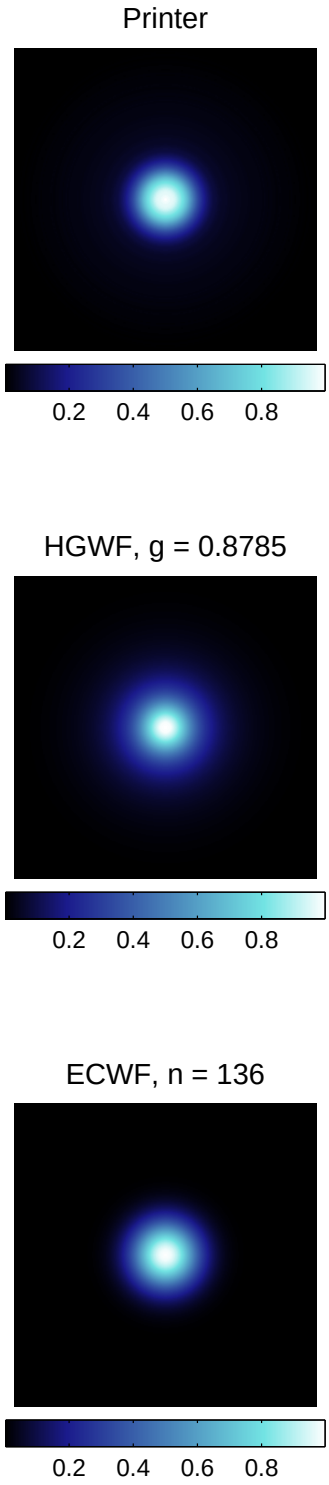

Figure 6.3: Orthogonal projections of scattering profiles, from Figure 6.1, corresponding to data obtained from printer paper using the red laser (633 nm) and its closest agreements using the HGWF and ECWF.

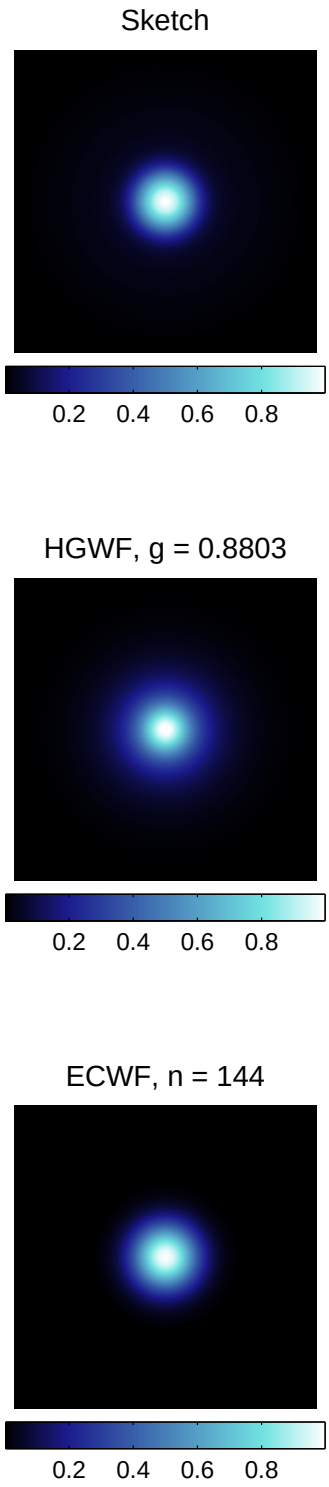

Figure 6.4: Orthogonal projections of scattering profiles, from Figure 6.1, corresponding to data obtained from sketch paper using the red laser (633 nm) and its closest agreements using the HGWF and ECWF.

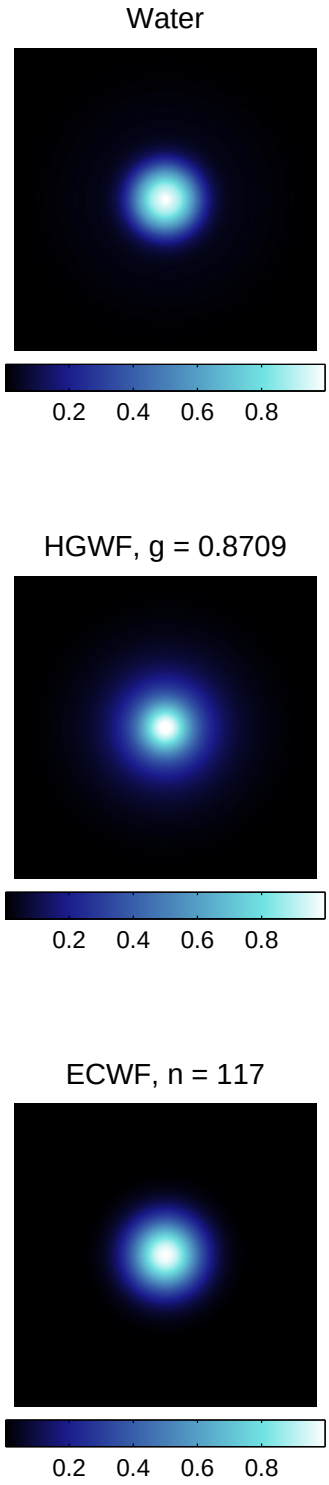

Figure 6.5: Orthogonal projections of scattering profiles, from Figure 6.1, corresponding to data obtained from water paper using the red laser (633 nm) and its closest agreements using the HGWF and ECWF.

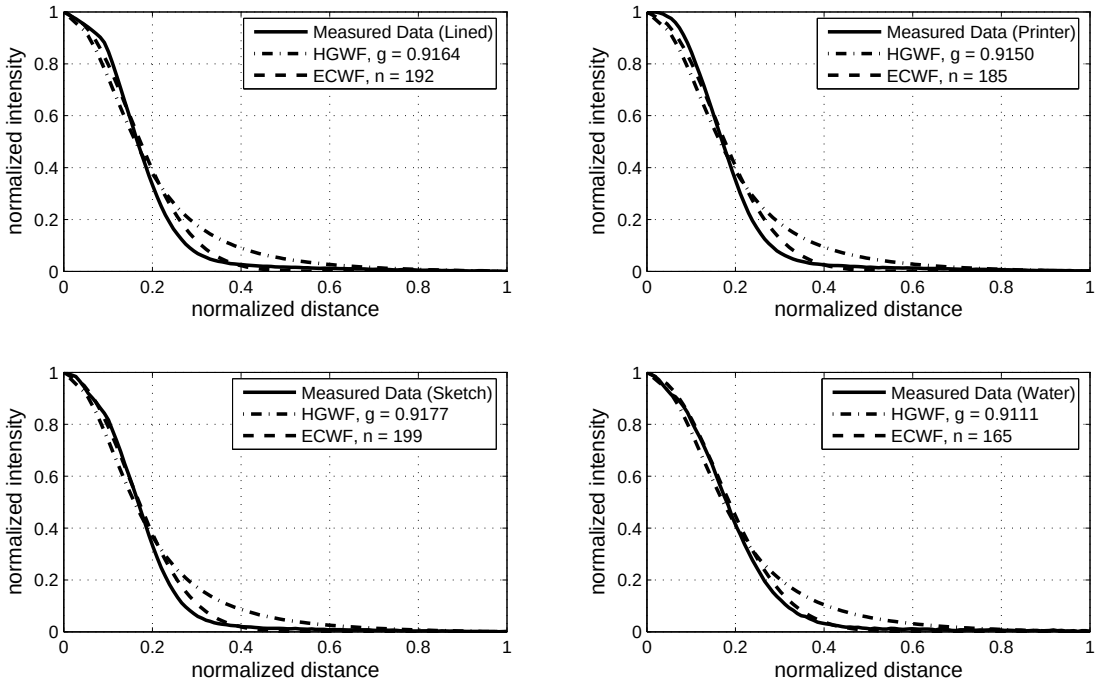

Figure 6.6: Comparison of measured data using the green laser (543 nm) and simulated scattering profiles obtained using the HGWF and ECWF that yield the closest agreements. Top left: lined paper. Top right: printer paper. Bottom left: sketch paper. Bottom right: water paper.

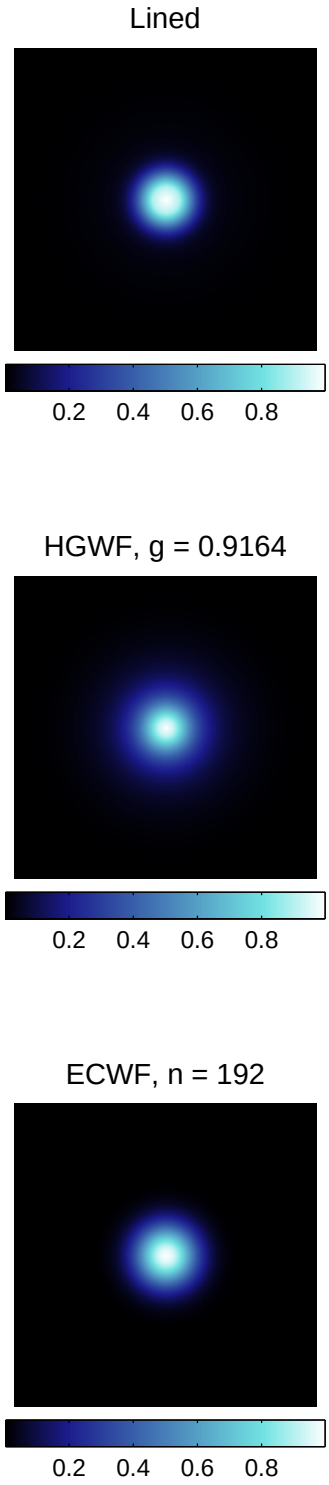

Figure 6.7: Orthogonal projections of scattering profiles, from Figure 6.6, corresponding to data obtained from lined paper using the green laser (543 nm) and its closest agreements using the HGWF and ECWF.

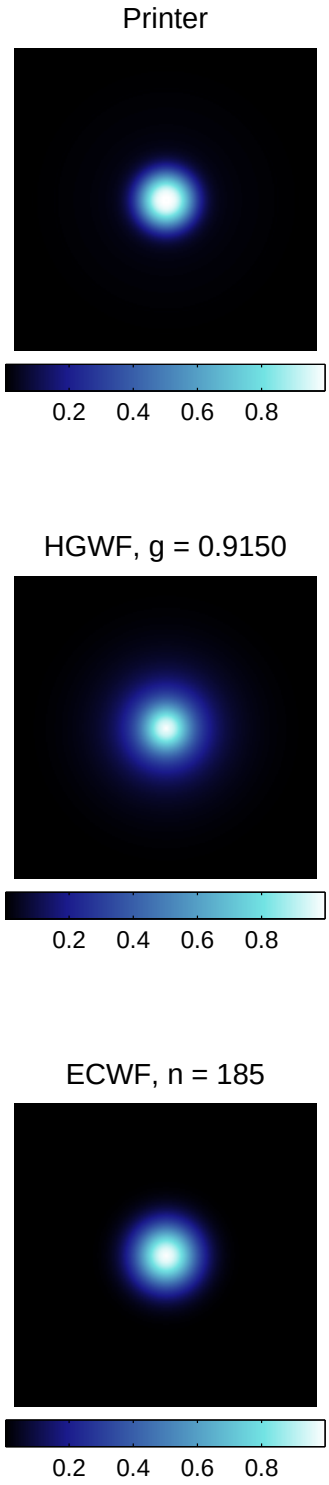

Figure 6.8: Orthogonal projections of scattering profiles, from Figure 6.6, corresponding to data obtained from printer paper using the green laser (543 nm) and its closest agreements using the HGWF and ECWF.

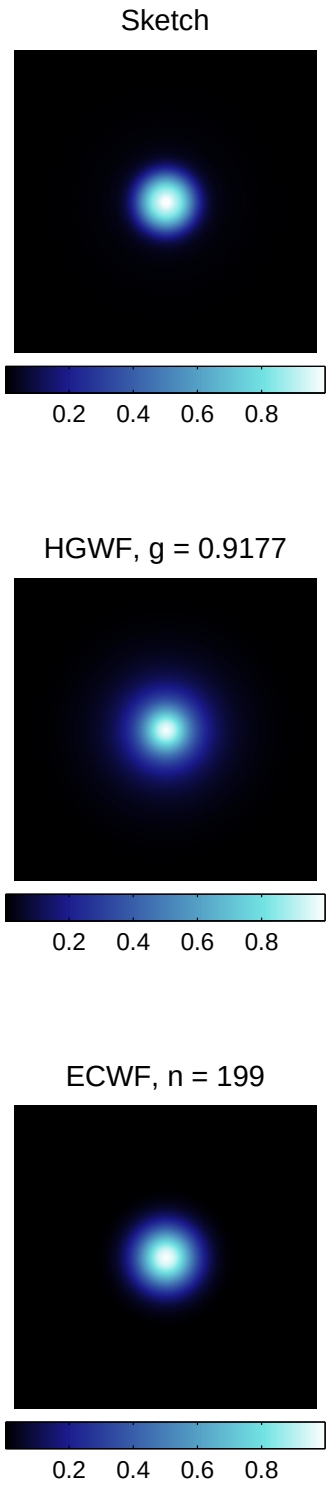

Figure 6.9: Orthogonal projections of scattering profiles, from Figure 6.6, corresponding to data obtained from sketch paper using the green laser (543 nm) and its closest agreements using the HGWF and ECWF.

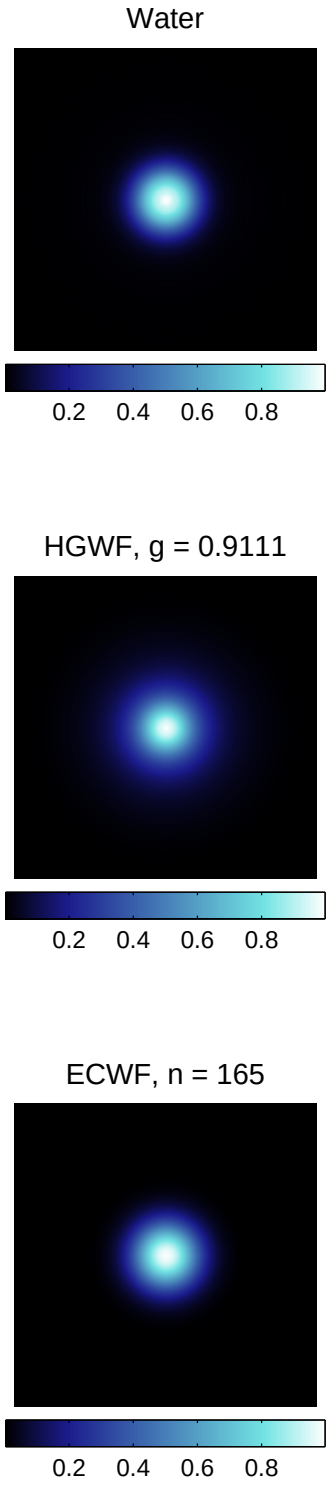

Figure 6.10: Orthogonal projections of scattering profiles, from Figure 6.6, corresponding to data obtained from water paper using the green laser (543 nm) and its closest agreements using the HGWF and ECWF.

Table 6.1: RMS errors associated with the approximations for the red laser (633 nm) corresponding to plots in Figures 4 and 6.

	Lined Paper	Printer Paper	Sketch Paper	Water Paper
HGWF	0.047342	0.043760	0.036203	0.044042
ECWF	0.026609	0.023730	0.018162	0.017780

Table 6.2: RMS errors associated with the approximations for the green laser (543 nm) corresponding to plots in Figures 5 and 7.

	Lined Paper	Printer Paper	Sketch Paper	Water Paper
HGWF	0.053489	0.057945	0.051973	0.042613
ECWF	0.025397	0.029789	0.021125	0.011227

Chapter 7

Conclusions

7.1 Alternative to the Henyey-Greenstein Function

Usually the choice of a function to approximate the bulk scattering of a paper's internal layers, either in stochastic [12] or deterministic [23] simulation frameworks, represents a compromise between accuracy and mathematical tractability. Such a compromise has motivated the use of the HG function in these frameworks. Although the experiments described in this paper were performed on whole samples, they suggest that, in the absence of measured data, the EC function may be a viable alternative for representing the bulk scattering of paper layers, notably for applications requiring a low level of accuracy (*e.g.*, visual inspection of computer generated images of translucent paper). However, for applications requiring a high level of accuracy (*e.g.*, prediction of paper properties using high sensitivity measurement data in conjunction with simulations), the degree of accuracy provided by both approximations may be below acceptable limits.

7.2 Predictability

We remark that the parameters of both functions, asymmetry factor g and directional exponent n, have no direct connection with the structural characteristics of paper. Addi-

tionally, the results show that the trend of the parameters could not be predicted based on the qualitative properties of the papers, namely thickness and transmission intensity. This limitation may prevent their selection to be quantitatively guided by the characterization data describing different samples, which, in turn, is likely to affect the predictability of models employing these functions.

One of the strategies to increase the predictability of the current modeling frameworks may involve the development of data driven approaches in which physically measured data can be directly incorporated into the simulations. Such approaches, however, are bound by data scarcity, which is one of the main reasons for the incorporation of bulk scattering approximations into models in the first place. Therefore, there is a need for more comprehensive measurements of paper optical properties that take into account not only the degree of non-uniformity in different types of paper, but also a broad range of measurement and environmental conditions. Such an undertaking will likely require a close collaborative effort between industry and academia. Future initiatives in this area should also include thorough studies on how the errors introduced by these approximations propagate through complex modeling frameworks.

7.3 Future Work

In light of the findings of this research, future work may involve the development of a predictive physically-based framework [27] for the simulation the optical properties of paper, with less reliance on "artificial" functions.

It has been noted that the macroscopic properties of paper are dictated by its microscopic structure. For example, non-uniform fiber orientation causes anisotropic reflectance [25]. The fibers in paper are also relatively transparent, but internal light scattering that occurs within these fibers causes paper to be relatively opaque. The properties of the fibers themselves, such as length, radius, and compression, also have different effects

on material density, and thus, optical properties [13]. A way to decrease the dependence on these functions is to model the physical microstructure of paper and apply Monte Carlo techniques to reproduce its macroscopic light reflection and transmission behaviors. However, the structure of fibers in paper is not clearly defined, introducing a large degree of complexity.

In order to adapt to this structural uncertainty, the modeling strategy must be flexible but preserving the physical characteristics of the material. One approach to be considered consists in generating fibers on the fly and discarding each one after an incident light beam intersects it, which has been successfully applied to the problem of light interacting with particulate materials [40]. This avoids the high cost of pre-computing and storing the complete discrete structure of the fibrous material. Additionally, it avoids the need in solving expensive ray-geometry intersection problems. Such an approach has not been used in this context before.

As future work, we plan to develop a predictive modeling framework using this stochastic approach. This framework may have applications not only in realistic image synthesis but also in applied optics and material science. For example, the framework may assist the pulp and paper industry in designing non-invasive optical techniques for quality control and material evaluation.

Bibliography

[1] ANSI. Nomenclature and definitions for illuminating engineering. In *ANSI/IES RP-6-1986*. Illuminating Engineering Society of North America, New York, 1986.

[2] Baird, P. K., and Irubesky, C. E. The determination of the volumetric composition of paper. *TAPPI 13* (May 1930), 274–277.

[3] Baranoski, G. Modeling the interaction of infrared radiation (750 to 2500nm) with bifacial and unifacial plant leaves. *Remote Sensing of Environment 100* (2006), 335–347.

[4] Baranoski, G., and Krishnaswamy, A. Simulation of light interaction with human skin. In *Eurographics 2005 - Tutorials* (2005), Eurographics Association, pp. 489–532.

[5] Baranoski, G., Krishnaswamy, A., and Kimmel, B. An investigation on the use of data-driven scattering profiles in Monte Carlo simulations of ultraviolet light propagation in skin tissues. *Physics in Medicine and Biology 49* (2004), 4799–4809.

[6] Baranoski, G., Krishnaswamy, A., and Kimmel, B. Increasing the predictability of tissue subsurface scattering simulations. *The Visual Computer 21*, 4 (2005), 265–278.

[7] Baranoski, G., and Rokne, J. *Light Interaction with Plants: A Computer Graphics Perspective*. Horwood Publishing, Chichester, UK, 2004.

[8] Bass, M., Ed. *Handbook of Optics*, 2^{nd} ed., vol. 1. McGraw-Hill, Inc., 1995.

[9] Béland, M., and Bennett, J. M. Effect of local microroughness on the gloss uniformity of printed paper surfaces. *Appl. Opt. 39*, 16 (2000), 2719–2726.

[10] Brakke, T., Smith, J., and Harnden, J. Bidirectional scattering of light from tree leaves. *Remote Sensing of Environment 29*, 2 (1989), 175–183.

[11] Bruls, W., and van der Leun, J. Forward scattering properties of human epidermal layers. *Photochemistry and Photobiology 40*, 2 (1984), 231–242.

[12] Carlsson, J., Persson, A., Persson, W., Wahlstrom, C.-G., Hellentin, P., and Malmqvist, L. Time-resolved studies of light propagation in paper. *Appl. Opt. 34*, 9 (1995), 1528–1535.

[13] Casey, J. *Pulp and Paper*, 2^{nd} ed., vol. 3. Interscience Publishers, Inc., New York, 1961.

[14] Casey, J. P. *Pulp and Paper*, 2nd ed., vol. 1. Interscience Publishers, Inc., New York, 1961.

[15] Chen, T. F., Baranoski, G., and Lin, K. F. Bulk scattering approximations for HeNe laser transmitted through paper. *Opt. Express 16*, 26 (2008), 21762–21771.

[16] Clewell, C. H. Scattering of light by pigment particles. *Journal of Optical Society of America 13* (August 1941), 521–527.

[17] Corte, H., and Kallmes, O. J. Statistical geometry of a fibrous network. In *The Formation and Structure of Paper*, F. Bolam, Ed., vol. 1. Technical Section of the British Paper and Board Makers' Association, 1962.

[18] Deng, M., and Dodson, C. T. J. *Paper: An Engineered Stochastic Structure*. TAPPI Press, 1994.

[19] Dorsey, J., Edelman, A., Jensen, H. W., Legakis, J., and Pedersen, H. K. Modeling and rendering of weathered stone. In *Proceedings of SIGGRAPH'99* (1999), pp. 225–234.

[20] Doughty, R. H. The relation of sheet properties and fiber properties in paper. *Paper Trade Journal 95*, 10 (September 1932), 111–118.

[21] E284-91C, A. S. Standard terminology of appearance. In *Physics-Based Vision Principles and Practice: Radiometry* (Boston, 1992), L. Wolff, S. Shafer, and G. Healey, Eds., Jones and Bartlett Publishers, pp. 146–161.

[22] Edström, P. Fast and stable solution method for angle-resolved light scattering simulation. Tech. Rep. R-02 35, Mid Sweden University, 2002.

[23] Edström, P. Comparison of the DORT2002 radiative transfer solution method and the Kubelka-Munk model. *Nordic Pulp and Paper Research Journal 19*, 3 (2004), 397–403.

[24] Gate, L. F. Light scattering in microporous materials using a photon diffusion model. *Journal of Physics D: Applied Physics* (1971), 837–846.

[25] Granberg, H., Jensen, J., and Mattsson, L. Forward scattering of fiber-containing surfaces studied by 3-D reflectance distribution simulations and measurements. *Optical Engineering 42*, 8 (2003), 2384–2390.

[26] Green, K., Lamberg, L., and Lumme, K. Stochastic modeling of paper structure and Monte Carlo simulation of light scattering. *Appl. Opt. 39*, 25 (2000), 4669–4683.

[27] Greenberg, D. P., Torrance, K. E., Shirley, P., Arvo, J., Lafortune, E. P., Ferwerda, J. A., Walter, B., Trumbore, B., Pattanaik, S. N., and Foo, S.-C. A framework for realistic image synthesis. In *SIGGRAPH* (1997), pp. 477–494.

[28] Hammerley, J., and Handscomb, D. *Monte Carlo Methods*. Wiley, New York, 1964.

[29] Hanrahan, P., and Krueger, W. Reflection from layered surfaces due to subsurface scattering. In *SIGGRAPH '93: Proceedings of the 20th annual conference on Computer graphics and interactive techniques* (New York, NY, USA, 1993), ACM, pp. 165–174.

[30] Harrison, V. G. W. Optical properties of paper. In *The Formation and Structure of Paper*, F. Bolam, Ed., vol. 1. Technical Section of the British Paper and Board Makers' Association, 1962.

[31] Henyey, L., and Greenstein, J. Diffuse radiation in the galaxy. *Astrophysics Journal 93* (1941), 70–83.

[32] Hunter, R., and Harold, R. *The Measurement of Appearance*, 2^{nd} ed. John Wiley & Sons, New York, 1987.

[33] Immel, D. S., Cohen, M. F., and Greenberg, D. P. A radiosity method for non-diffuse environments. In *SIGGRAPH '86: Proceedings of the 13th annual conference on Computer graphics and interactive techniques* (New York, NY, USA, 1986), ACM, pp. 133–142.

[34] Irvin, W. M. Multiple Scattering by Large Particles. *Astrophysical Journal 142* (Nov. 1965), 1563–1575.

[35] Ishimaru, A. *Wave Propagation and Scattering in Random Media*, 2^{nd} ed., vol. 1. Academic Press, 1978.

[36] Jacques, S., Alter, C., and Prahl, S. Angular dependence of HeNe laser light scattering by human dermis. *Lasers in Life Sciences 1*, 4 (1987), 309–333.

[37] Jensen, H. W., Durand, F., Stark, M. M., Premoze, S., Dorsey, J., and Shirley, P. A physically-based night sky model. In *Proceedings of SIGGRAPH'2001* (2001), pp. 399–408.

[38] Jensen, H. W., Legakis, J., and Dorsey, J. Rendering of wet materials. In *Rendering Techniques '99* (1999), pp. 273–282.

[39] Kattawar, G. W. A three-parameter analytic phase function for multiple scattering calculations. *Journal of Quantitative Spectroscopy and Radiative Transfer 15* (1975), 839–849.

[40] Kimmel, B., and Baranoski, G. A novel approach for simulating light interaction with particulate materials: application to the modeling of sand spectral properties. *Optics Express 15*, 15 (2007), 9755–9777.

[41] Krishnaswamy, A., Baranoski, G., and Rokne, J. Improving the reliability/cost ratio of goniophotometric comparisons. *Journal of Graphics Tools 9*, 3 (2004), 1–20.

[42] Lettieri, T., Marx, E., Song, J., and Vorburger, T. Light scattering from glossy coatings on paper. *Appl. Opt. 30*, 30 (1991), 4439.

[43] Lewis, R. R. Making shaders more physically plausible. In *In Fourth Eurographics Workshop on Rendering* (1993), pp. 47–62.

[44] Li, Z., Fung, A., Tjuatja, S., Gibbs, D., Betty, C., and Irons, J. A modeling study of backscattering from soil surfaces. *IEEE Transactions on Geoscience and Remote Sensing 34*, 1 (January 1996), 264–271.

[45] Mourant, J., Freyer, J., Hielscher, A., Eick, A., Shen, D., and Johnson, T. Mechanisms of light scattering from biological cells relevant to noninvasive optical-tissue diagnostics. *Applied Optics 37*, 16 (June 1998), 3586–3593.

[46] Neuman, M. Anisotropic reflectance from paper - measurements, simulations and analysis. Master's thesis, Department of Physics, UMEA University, 2005.

[47] Oksman, A., Silvennoinen, R., Peiponen, K., Avikainen, M., and Komulainen, H. Reflectance study of compressed paper. *Appl. Spectrosc. 58*, 4 (2004), 481–485.

[48] Phong, B. T. Illumination for computer generated pictures. *Commun. ACM 18*, 6 (1975), 311–317.

[49] Prahl, S. *Light Transport in Tissue*. PhD thesis, University of Texas at Austin, 1988.

[50] Prahl, S., Keijzer, M., Jacques, S., and Welch, A. A Monte Carlo model of light propagation in tissue. *SPIE Institute Series IS 5* (1989), 102–111.

[51] Prahl, S., van Gemert, M., and Welch, A. Determining the optical properties of turbid media by using the adding-doubling method. *Appl. Opt. 32* (1993), 559–568.

[52] Shirley, P. S. *Physically Based Lighting Calculations for Computer Graphics*. PhD thesis, University of ILlinois at Urbana-Champaign, 1991.

[53] Spiegel, M. *Schaum's Outline of Theory and Problems of Statistics*, 2^{nd} ed. Schaum's outline series. McGraw-Hill, Inc., 1991.

[54] Stam, J. An illumination model for a skin layer bounded by rough surfaces. In *In Proceedings of the 12th Eurographics Workshop on Rendering Techniques* (2001), Springer-Verlag, pp. 39–52.

[55] Stover, J. C. *Optical Scattering: Measurement and Analysis*. McGraw-Hill, Inc., 1990.

[56] Tuchin, V. *Tissue Optics: Light Scattering Methods and Instruments for Medical Diagnosis*, 2^{nd} ed. SPIE Publications, 2007.

[57] Uesugi, A., Irvine, W. M., and Kawata, Y. Formation of absorption spectra by diffuse reflection from a semi-infinite planetary atmosphere. *Journal of Quantitative Spectroscopy and Radiative Transfer 11* (1971), 797–808.

[58] van Gemert, M., Jacques, S., Sterenborg, H., and Star, W. Skin optics. *IEEE Transactions on Biomedical Engineering 36*, 12 (Dec. 1989), 1146–1154.

[59] Witt, A. N. Multiple scattering in reflection nebulae. I - A Monte Carlo approach. *The Astrophysical Journal Supplement Series 35* (Sept. 1977), 1–6.

[60] Yoon, G., Welch, A., Motamedi, M., and Gemert, M. Development and application of three-dimensional light distribution model for laser irradiated tissue. *Quantum Electronics, IEEE Journal of 23*, 10 (Oct 1987), 1721–1733.

Index

Appendix A

Measurement of Light Spatial Distribution

The measurement of light spatial distribution is usually performed using goniophotometers [32]. A goniophotometer is an instrument that measures radiant flux as a function of angles of illumination and observation. More specifically, they are employed in the measurement of light reflected and/or transmitted by different materials under different lighting conditions. The light flux, which is incident on the sample from an emitter, interacts with the specimen and the reflected and/or transmitted light is then captured by a detector. Measurements can be obtained in different ways, using different geometries of illumination and observation. Figure A.1 is a sketch illustrating the key components of a goniophotometer set-up for the measurement of transmittance profiles. These instruments are important tools for fundamental research in many different fields that require optical measurements, ranging from colorimetry to remote sensing [41]. Needless to say, paper science also benefits from this technology [25].

A comprehensive goniophotometric record for a material requires a sizeable number of measurements. Both the emitter and detector need to be moved independently of one another to all possible positions on a hemisphere centered around the specimen to be

studied. To cover a complete hemisphere (2π steradians) with minimal overlap, about a thousand distinct positions are required [41]. Then, a thousand radiance readings would be needed for each of the one thousand illumination positions. Therefore, to capture the full range of goniometric data, one million measurements would be required.

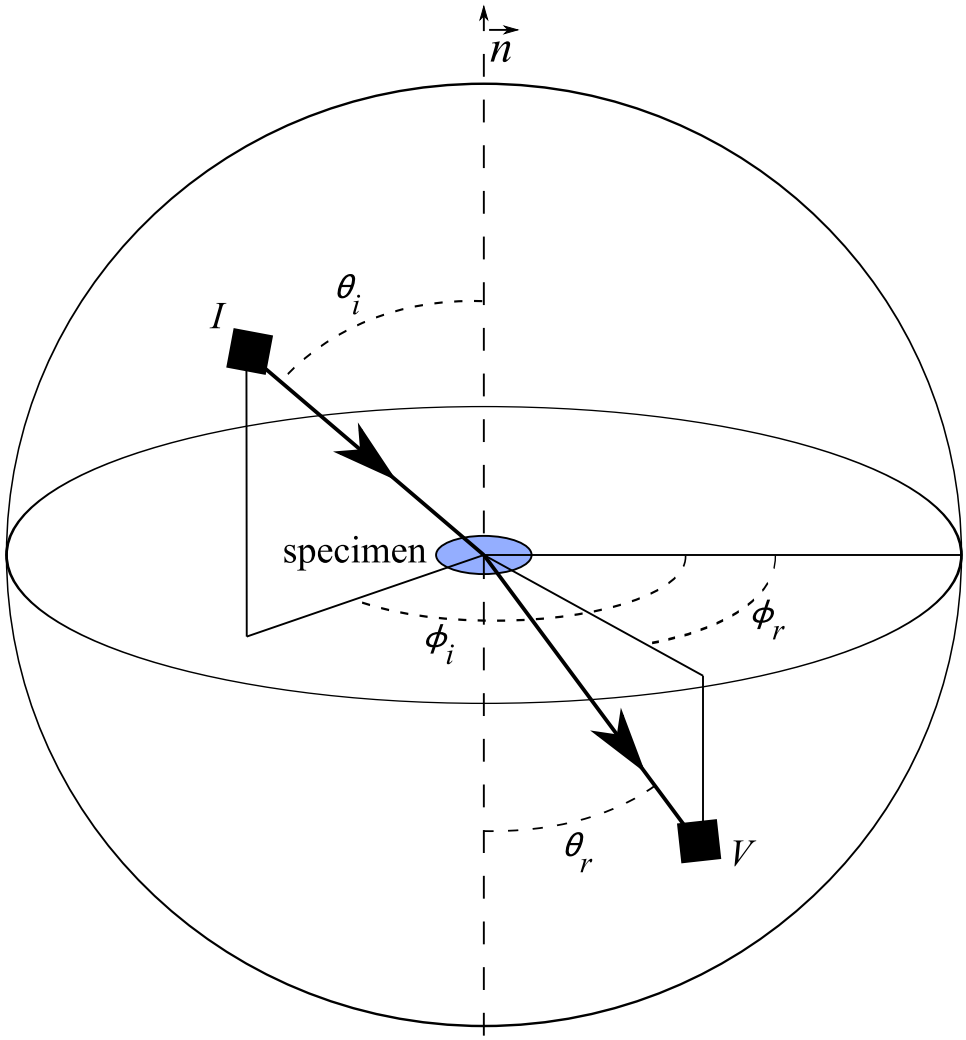

Figure A.1: A sketch of the key components of a goniophotometer used for measuring spatial distribution of transmitted light. The specimen normal is represented by $\vec{n}$. The emitter casts light from patch I at a polar angle of θ_i and azimuthal angle of ϕ_i. A radiance sensor detects the transmitted light at a patch V at a polar angle of θ_r and azimuthal angle of ϕ_r.

Appendix B

Bidirectional Transmittance Distribution Function

The bidirectional transmittance distribution function (BTDF) is one of the physical properties that can be measured by a goniophotometer and is the format of the simulated data collected in this thesis. The mathematical definition of the BTDF, with light incident from the solid angle $\vec{\omega_i}$ and detector's location corresponding to the solid angle $\vec{\omega_r}$, is

$$f_t(\vec{\omega_i}, \vec{\omega_r}) = \frac{\Phi_r}{\Phi_i \vec{\omega_r}^p},$$

where Φ_r is the transmitted flux that hits the detector, Φ_i is the incident flux and $\vec{\omega_r}^p$ is the adjusted solid angle corresponding to the direction of the detector. Additionally, the adjusted solid angle is given by

$$\vec{\omega_r}^p = \frac{A_r \ \cos\theta_r}{L^2},$$

with A_r being the area of the radiance detector, L being the distance between the specimen and the radiance detector or equivalently the radius of the collecting hemisphere, and θ_r being the polar angle between with the radiance detector and the specimen normal, as labeled in Figure A.1.

Assuming the incident light with radiant flux Φ_i is simulated by N_i rays in a virtual goniophotometer, each with power Φ_{ray}, then the total incident flux can be rewritten as

$$\Phi_i = N_i \Phi_{ray}.$$

Similarly, the received flux can be written as

$$\Phi_r = N_r \Phi_{ray},$$

whereN_r is the number of rays reaching the detector. Then, the expression for the BTDF reduces to

$$f_t(\vec{\omega_i}, \vec{\omega_r}) = \frac{N_r}{N_i \vec{\omega_r}^p}.$$

Similar analogues can be defined for the reflectance by having the detector placed in the upper hemisphere.